Proceedings of ALGORITMY 2024
pp. 11–20

AUTOMATED COMPLETION OF SEGMENTED FRAGMENTS OF MACROPHAGES USING WEIGHTED DILATION AND EROSION IN 2D+TIME MICROSCOPY VIDEOS*

SEOL AH PARK† AND KAROL MIKULA ‡

Abstract. This paper presents a method for automated completion of segmented fragments in 2D+time microscopy movies. This method aims to automatically and accurately compute morphological features for segmented macrophages that are critical for understanding their phenotypic characteristics. In the situation that segmentation results in fragments corresponding to a single macrophage, it becomes challenging to determine whether these fragments belong to the same macrophage. Consequently, it is essential to complete the fragments for accurate quantitative analysis of morphology. To achieve this, we propose a method based on weighted dilation and erosion (WDE) in the level-set formulation. By regulating the speed of the level lines based on local image intensity and thresholds calculated from the local Otsu's method, this approach effectively integrates fragmented segments while preserving the overall macrophage shape. The efficacy of the method is demonstrated through both visual and quantitative assessments, which indicate its ability to accurately complete segmented macrophages across a range of shapes and intensity levels in the images. Furthermore, the method has been shown to improve the accuracy of quantitative assessments when compared to ground truth images.

Key words. Macrophage, Image segmentation, Image dilation, Image erosion, Level-set method

AMS subject classifications. 68U10, 92-08, 92C55

1. Introduction.

The morphological characteristics of macrophages have been identified as important factors that distinguish between different phenotypes and functions [1] at the two extremes of polarization, known as the M1 and M2 states [3]. Macrophages in the M1 state are implicated in pro-inflammatory responses typically observed during the early stages of inflammation [4]. As inflammation resolves, M1 macrophages switch to the M2 state, which orchestrates anti-inflammatory responses to facilitate tissue repair and remodeling [5]. With regard to the morphological differences between the two states, M1 macrophages are characterized by a rounded and flat shape, while M2 macrophages exhibit elongated and complex morphologies.

Quantitative analysis of morphological features in microscopy videos can contribute to studying the differences in shape between M1 and M2 macrophages, as well as their changing morphologies over time. This typically involves two processes. First, cell tracking identifies the centers of individual macrophages over time. Second, based on a detected center, the morphological features of the corresponding segmented cells are measured to ensure accurate computations for all individual macrophages. This approach is accurate when there are no segmented fragments; here, segmented fragments mean that image segmentation results in multiple disconnected pieces corresponding to a single macrophage. For instance, there are three fragments in the bottom-right of Fig. 1.1 that belong to a single macrophage as shown in the original

*This work was supported by Grant APVV-19-0460, APVV-23-0186, VEGA 1/0249/24, and Marie Skłodowska-Curie Actions under grant agreement ID 955576.

†Department of Mathematics and Descriptive Geometry, Slovak University of Technology in Bratislava, Radlinskeho 11, Bratislava, 810 05, Slovakia (seol.park@stuba.sk).

‡Department of Mathematics and Descriptive Geometry, Slovak University of Technology in Bratislava, Radlinskeho 11, Bratislava, 810 05, Slovakia (karol.mikula@stuba.sk).

image (top panel). From the result of cell tracking, the center of the macrophage is designated also as one of the small fragments. Consequently, the perimeter, area, and other measurements for this macrophage become very small at this time moment if we measure them for one connected segmented cell. To resolve this, the completion of fragmented segments corresponding to the same macrophage is needed. We use the dilation-erosion process using the level-set approach [6, 7], which involves expanding and contracting level lines along fragment boundaries to fill gaps or missing edges. This method involves the evolution of level lines in the normal direction – either outward or inward – only determined by the sign of the velocity. Initially, the level lines associated with fragment boundaries undergo expansion and adhesion (dilation), followed by a subsequent phase of contraction (erosion) once the fragments are fully connected. However, within the image domain, some segmented cells exist that do not require this expansion-contraction process (see the second row of Fig. 3.2). Applying uniform dilation-erosion speeds across all pixels risks distorting the shapes of already completed segmented cells. Hence, we introduce varying speeds for each pixel depending on whether a pixel is located near either a fragment or an already completed cell. Specifically, we utilize image thresholds computed from local Otsu's method for all pixels, which allows us to assign faster speeds to pixels near fragments and slower speeds to those near completed cells. By integrating these evolving speeds into the level-set equation, the so-called weighted dilation-erosion approach ensures the accurate completion of fragments while preserving the shapes of existing segmented cells. Note that the method proposed in the paper serves as a post-processing step in segmentation, particularly in the context of the segmentation pipeline, corresponding to filtering, local Otsus's method, and subjective surface, segmentation suggested in [10].

The dataset presented in this paper corresponds to that of [10], employing a three-day-old transgenic zebrafish larva (Tg(mpeg1:Gal4/-UAS:Kaede)) and imaging it with a spinning disk confocal microscope.

The structure of this paper is as follows. Section 2 describes the mathematical model. In Section 3, visual and quantitative assessments are presented. Finally, we discuss the advantages and limitations of the proposed model and conclude the paper.

2. Mathematical and numerical methods. In this section, first, the mathematical expression and its numerical discretization of the level-set equation will be presented. Then, the level-set equation with the varying speed of each pixel will be presented.

2.1. Level-set method. The level-set equation for the motion of level lines in a normal direction representing dilation and erosion is written as

$$\frac{\partial u}{\partial t} + \mu|\nabla u| = 0, \tag{2.1}$$

where t denotes the scale, the amount of evolution of level lines, $u(t, x_1, x_2)$ is the unknown real function which is defined on $[0, T_F] \times \Omega$, $\mathbf{x} = (x_1, x_2) \in \Omega \subset R^2$, and μ is a constant.
The initial condition is given by

$$u(0, \mathbf{x}) = u^0(\mathbf{x}) \tag{2.2}$$

and it corresponds to a binarized image obtained from image segmentation.

Let us denote by $u^n_{i,j}$ a numerical solution at the pixel (i, j) in n^{th} discrete step

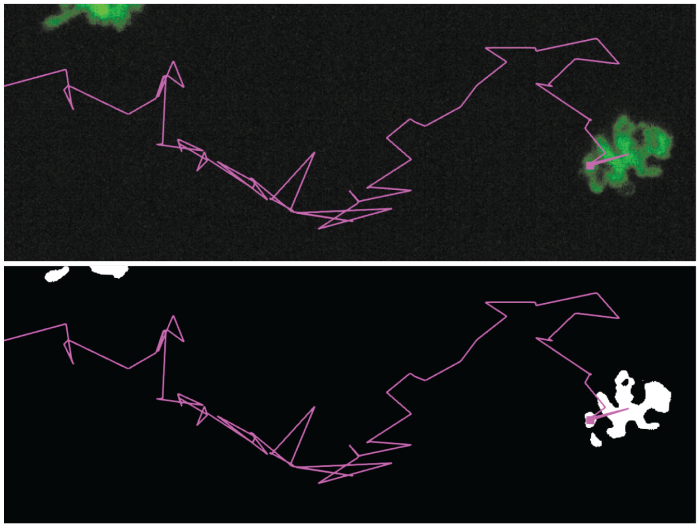

FIG. 1.1. *Original (top) and segmented image (bottom) with a macrophage trajectory (pink line)*

$n\tau$ with step size τ. Then, Equation (2.1) is discretized in time as

$$\frac{u_{i,j}^{n+1} - u_{i,j}^{n}}{\tau} = -\mu|\nabla u_{i,j}^{n}|. \tag{2.3}$$

By using the upwind scheme, the norm of the gradient of u in the n^{th} evolution step for a pixel (i, j) is computed as [8]

$$\begin{aligned} |\nabla^{\pm} u_{i,j}^{n}| = [&\max\{\max(D^{\mp\alpha} u_{i,j}^{n}, 0), \text{-min}(D^{\mp\alpha} u_{i,j}^{n}, 0)\}^2 + \\ &\max\{\max(D^{\mp\beta} u_{i,j}^{n}, 0), \text{-min}(D^{\mp\beta} u_{i,j}^{n}, 0)\}^2]^{1/2}, \end{aligned} \tag{2.4}$$

where

$$\begin{aligned} D^{\pm\alpha} u_{ij}^{n} &= \pm\frac{1}{h}(u_{i\pm1,j} - u_{i,j}), \\ D^{\pm\beta} u_{i,j}^{n} &= \pm\frac{1}{h}(u_{i,j\pm1} - u_{i,j}), \end{aligned} \tag{2.5}$$

and h denotes the pixel size. Finally, Equation (2.1) is discretized as follows.

$$u_{i,j}^{n+1} = u_{i,j}^{n} - \tau[\max(\mu, 0)\nabla^{+} u_{i,j}^{n} + \min(\mu, 0)\nabla^{-} u_{i,j}^{n}]. \tag{2.6}$$

Dilation and erosion occur when $\mu < 0$ and $\mu > 0$, respectively.

2.2. Weighted dilation and erosion. The thresholds obtained from the local Otsu's method are used to control the speed of the evolving level lines for every pixel. The local Otsu's method is the classical Otsu's method [9] restricted to a window

centered at a pixel (i,j), providing the optimal threshold T_r^* for the pixel (i,j). A comprehensive mathematical explanation can be found in [10].

Let $I_{i,j}$ represent the image intensity of the original image at pixel (i,j), and $T_{i,j}^*$ denote the computed optimal threshold at the same pixel, where $T_{i,j}^* \in [0,1]$ and $I_{i,j} \in [0,1]$. Based on the image segmentation workflow outlined in the paper[10], pixels situated between fragments tend to exhibit low image intensities, resulting in a uni-modal distribution characterized by a single peak, within the local window (see the second row of Fig. 3.1). Therefore, the computed threshold $T_{i,j}^*$ closely positions with the image intensity $I_{i,j}$ in the histogram. On the other hand, within the local window depicted in the first row of Fig. 3.1, the part of the macrophage exhibits substantially higher image intensity compared to the background, leading to a significant deviation of $T_{i,j}^*$ from $I_{i,j}$. We will use this property to determine the evolution speed of each pixel along the level lines.

From Equation (2.6), the speed at a pixel (i,j) in the normal direction can be rewritten as

$$\mu \to \pm v_{i,j}, \quad v_{i,j} = \frac{1}{2}(\tilde{S}_{i,j} + I_{i,j}), \tag{2.7}$$

where $\pm$ denotes erosion $(+)$ and dilation $(-)$, and $\tilde{S}_{i,j} = 1 - |I_{i,j} - T_{i,j}^*|$. As mentioned above, a darker pixel (i,j) with a small value of $|I_{i,j} - T_{i,j}^*|$ is likely to be inside a macrophage, but is not detected as a part of a macrophage, thus requiring completion. While, pixel (i,j) with a large value of $|I_{i,j} - T_{i,j}^*|$ is more likely to be positioned in the background but close to an already fully segmented cell where significant evolution is undesirable. As a result, $\tilde{S}_{i,j}$ will have a high value in the former case and a low value in the latter. Finally, the addition of $I_{i,j}$ to the speed, as illustrated in Equation (2.7), results in a deceleration of the evolution of the level lines as they approach the background due to the low image intensity of the background. From this point, we will refer to the dilation and erosion with different speeds for each pixel as "weighted dilation and erosion". Furthermore, we add the small effect of curvature, κ, for regularization. The curvature κ with finite difference approximations is computed as follows.

$$\begin{aligned} \kappa &= -\frac{u_{xx}u_y^2 - 2u_x u_y u_{xy} + u_{yy}u_x^2}{|\nabla u|^3}, \\ u_x &= \frac{1}{2h}(u_{i+1,j} - u_{i-1,j}), \quad u_y = \frac{1}{2h}(u_{i,j+1} - u_{i,j-1}), \\ u_{xx} &= \frac{1}{h^2}(u_{i+1,j} - 2u_{i,j} + u_{i-1,j}), \quad u_{yy} = \frac{1}{h^2}(u_{i,j+1} - 2u_{i,j} + u_{i,j-1}), \\ u_{xy} &= \frac{1}{4h^2}(u_{i+1,j+1} - u_{i-1,j+1} - u_{i+1,j-1} + u_{i-1,j-1}). \end{aligned} \tag{2.8}$$

The discrete formulation of weighted dilation and erosion is described as

$$u_{i,j}^{n+1} = u_{i,j}^n - \tau[\max(F,0)\nabla^+ u_{i,j}^n + \min(F,0)\nabla^- u_{i,j}^n], \tag{2.9}$$

where $F = \pm v_{i,j} + \epsilon\kappa$. Here, $v_{i,j}$ denotes the normal speed for each pixel (i,j) in accordance with Equation (2.7) with the negative for dilation, and positive sign for erosion, respectively. The term of $\epsilon\kappa$ is the curvature effect multiplied by a small constant, $\epsilon \ll 1$. In this study, we select the values of the parameters $\epsilon = 0.01$, $h = 1$, and $\tau = 0.25$.

3. Result.

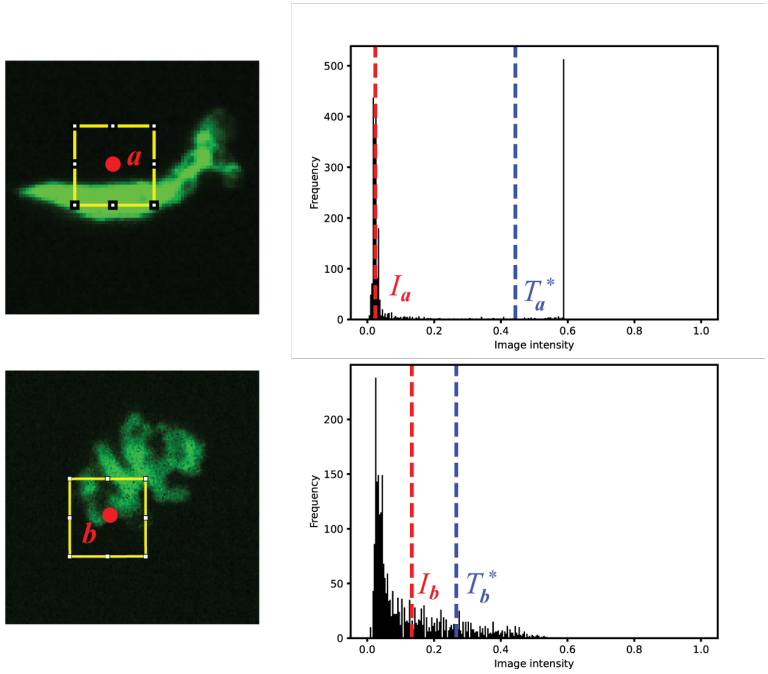

FIG. 3.1. *Images and histograms evaluated in local windows (yellow) are displayed. The first row shows a local window centered on pixel* $\boldsymbol{a}$*, accompanied by the corresponding histogram. Similarly, the second row displays a window centered on pixel* $\boldsymbol{b}$ *along with its histogram. Here,* $I_{\boldsymbol{a}}$ *and* $I_{\boldsymbol{b}}$ *represent the image intensities at pixels* $\boldsymbol{a}$ *and* $\boldsymbol{b}$*, respectively. The computed thresholds are denoted as* $T^*_{\boldsymbol{a}}$ *and* $T^*_{\boldsymbol{b}}$*.*

3.1. Visual assessment of weighted dilation and erosion. In this section, we illustrate the results of the dilation and erosion processes, both with and without considering different speeds of level lines at individual pixels. For comparison, we examine two macrophages with contrasting characteristics: one exhibits a bright macrophage intensity and simple shapes, yielding a well-segmented shape, while the other displays weaker macrophage intensity and complex shapes, resulting in segmented fragments.

To see the difference of $|I_{i,j} - T^*_{i,j}|$ between these two macrophages, in Fig. 3.1, we present the image histogram within local windows, denoted by yellow squares, centered on the pixels $\boldsymbol{a}$ and $\boldsymbol{b}$. The pixel $\boldsymbol{a}$ is in the background near the bright area of the macrophage, causing the histogram to display bi-modality. It means that the computed threshold $T^*_{\boldsymbol{a}}$ is significantly distant from the image intensity $I_{\boldsymbol{a}}$ at pixel $\boldsymbol{a}$. Conversely, in the local window centered on the pixel $\boldsymbol{b}$ located between the fragments (see Fig. 3.1), the computed threshold $T^*_{\boldsymbol{b}}$ is close to the image intensity $I_{\boldsymbol{b}}$. Therefore, the value of $|I_{\boldsymbol{a}} - T^*_{\boldsymbol{a}}|$ is larger than $|I_{\boldsymbol{b}} - T^*_{\boldsymbol{b}}|$, resulting in slower movement of level lines at $\boldsymbol{a}$ compared to $\boldsymbol{b}$. The parameters for the local Otsu's method to compute $T^*_{\boldsymbol{a}}$ and $T^*_{\boldsymbol{b}}$ are selected from the aforementioned paper [10].

In Fig. 3.2, the red lines show the boundaries of the two macrophges after dilation with the same number of iterations (= 30) for cases of three different speeds. The first column is the original image, while the second, third, and fourth columns

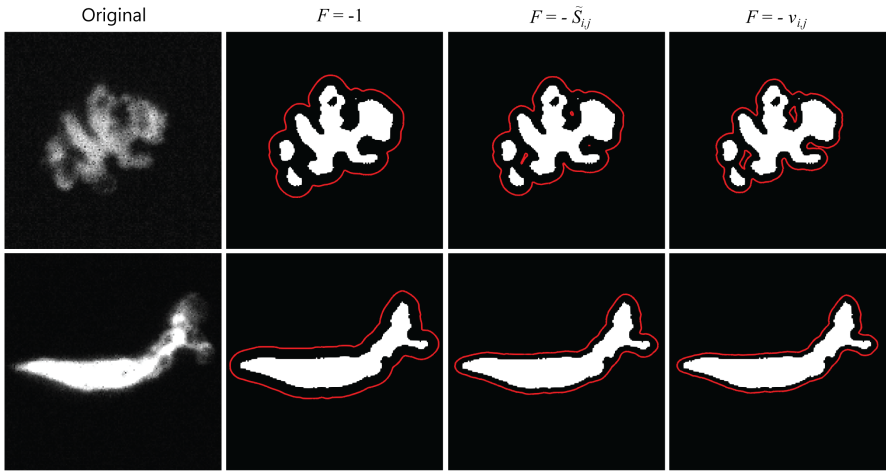

FIG. 3.2. *Boundaries (depicted by red lines) after applying dilation with three different speeds of the level-set equation. The first column shows the original images of two macrophages. The second column displays boundaries after dilation with a constant speed. In the third column, boundaries after dilation with the speed* $-\tilde{S}_{i,j} = -1 + |I_{i,j} - T^*_{i,j}|$*, are illustrated. Lastly, the fourth column exhibits boundaries after dilation with the speed* $-v_{i,j} = -\frac{1}{2}(\tilde{S}_{i,j} + I_{i,j})$*. Here,* $I_{i,j}$ *and* $T^*_{i,j}$ *denote the image intensity and computed threshold at a pixel* (i, j)*, respectively. The number of iterations of level lines is set to* 30*.*

are the results when the speed F is constant, $-\tilde{S}_{i,j}$, and $-v_{i,j}$, respectively. When $F = -1$, the expansion speed is uniform for both macrophages, and the high curvature regions of the macrophage in the first row disappear. However, when different speeds in individual pixels are considered, the amount of expansion is different for the two macrophages. In addition, the high curvature parts remain as holes in the third and fourth columns, thereby allowing for the preservation of high curvature parts when attempting erosion. Particularly in the fourth column, the high curvature parts correspond better to the original image $I_{i,j}$.

Starting with the boundaries denoted by red in Fig. 3.2, erosion is performed with the same number of iterations for cases of three different speeds. As illustrated in Fig. 3.3, the top panel of the second column shows that macrophages with complex shapes are oversimplified, as the high curvature regions are eliminated during dilation. In contrast, erosion with $F = v_{i,j}$ gives accurate boundaries in both cases. In addition, the boundary for the macrophage in the second row is closer to the original when using $F = v_{i,j}$ compared to $F = 1$ and $F = \tilde{S}_{i,j}$.

3.2. Quantitative assessment of weighted dilation and erosion. This section presents measurements of morphological features, including perimeter, area, and circularity (calculated as $4\pi * \text{area}/\text{perimeter}^2$) for two segmented macrophages over time with the application of weighted dilation and erosion (hereafter referred to as WDE). In addition, we compare these measurements to results obtained from ground truth and to results obtained before the application of WDE. Fig. 3.4 and 3.5 illustrate the morphological features, including perimeter (top-left), area (top-center),

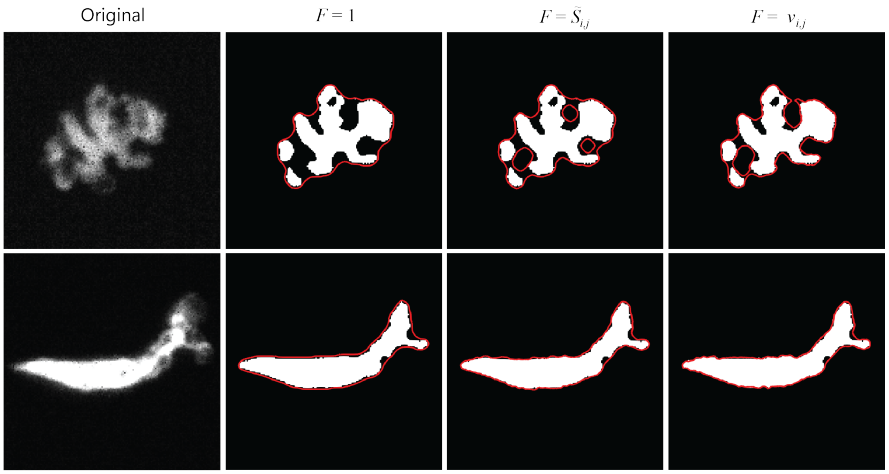

FIG. 3.3. *Boundaries (depicted by red lines) after the erosion with three different speeds starting from the dilated images in Fig. 3.2. The first column shows the original images of two macrophages. The second column displays boundaries after erosion with a constant speed. In the third column, boundaries after erosion with the speed* $\tilde{S}_{i,j} = 1 - |I_{i,j} - T^*_{i,j}|$*, are illustrated. Lastly, the fourth column exhibits boundaries after erosion with the speed* $v_{i,j} = \frac{1}{2}(\tilde{S}_{i,j} + I_{i,j})$*. Here,* $I_{i,j}$ *and* $T^*_{i,j}$ *denote the image intensity and computed threshold at a pixel* (i, j)*, respectively. The number of iterations of level lines is set to* 30*.*

and circularity (top-right), calculated from ground truth (shown in green), before applying WDE (shown in blue), and after applying WDE (shown in red).

The way of computing morphological features is as follows: utilizing the results of cell tracking [10], we identify the centers of segmented regions, representing connected subregions within the segments. Perimeter, area, and circularity are then computed solely within the respective segmented regions. For instance, in the scenario presented in the second row of the third column in Fig. 3.4, two centers corresponding to two segmented regions are obtained. However, only one center is chosen to represent the macrophage's location, resulting in morphological features being computed for approximately half the original area.

For a detailed comparison, we select four time moments denoted as i, ii, iii, and iv of the two inspected macrophages and visually assess the corresponding segmented shapes in comparison to the original images. Before the application of WDE, the areas at these selected time points are notably smaller than those computed from ground truth, indicating the presence of fragmented segments, as shown in the "Before WDE" row. After the application of WDE, all three morphological features are much more similar to the ground truth results. This is evident in the "After WDE" row, where all segmented fragments are integrated, preserving the overall shapes of the macrophages.

The morphology of the macrophages shown in Fig. 3.5 is more complex compared to those in Fig. 3.4. To highlight the performance of WDE, we selected four specific time points as before. The areas corresponding to these time points are smaller

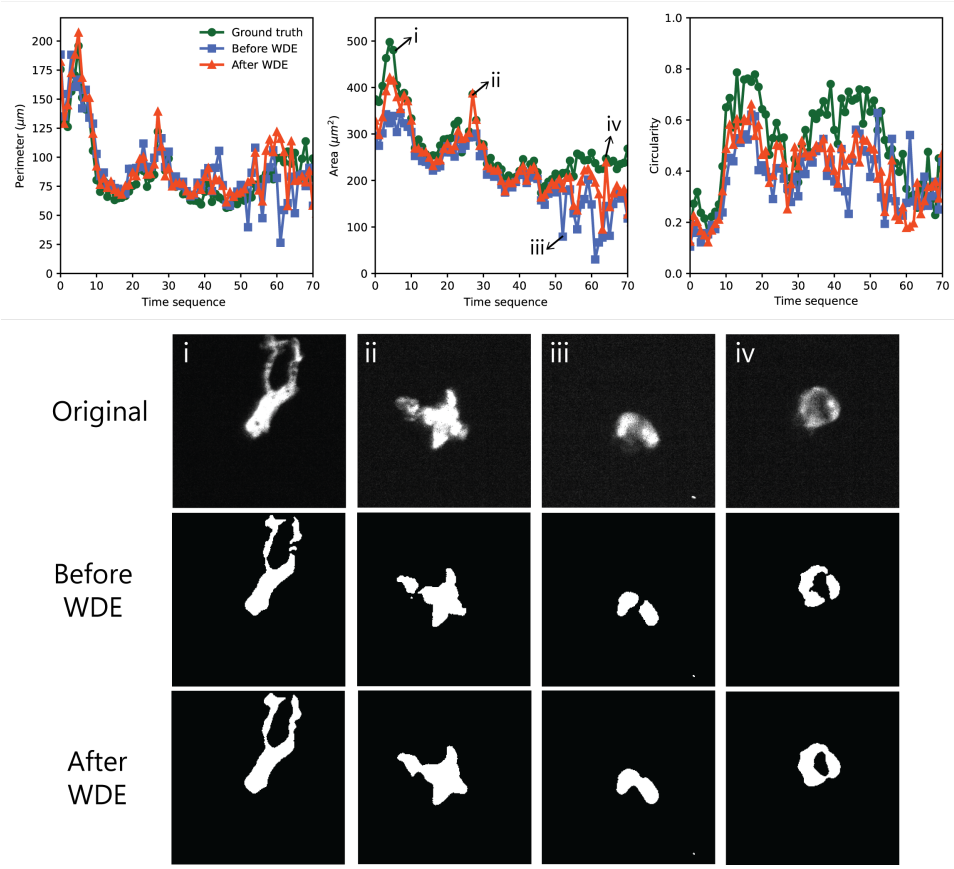

FIG. 3.4. *Morphological characteristics such as perimeter, area, and circularity are calculated over time for a macrophage exhibiting relatively round shapes. Four time points, labeled as* i, ii, iii, iv*, are chosen to compare the segmented shapes before and after the application of weighted dilation and erosion.*

than those computed from the ground truth before the application of WDE. In particular, in cases *ii* and *iv*, the areas are significantly small compared to the ground truth. This is mainly because the positions of the detected centers obtained from cell tracking are within a very small segmented region, and morphological features are computed only within these limited regions. After applying WDE, all segmented fragments are effectively completed, allowing for a more accurate quantitative evaluation. However, there are cases where the regions after applying WDE yield higher values than the ground truth, especially in cases involving complex shapes, because the smoothing effect of WDE tends to mitigate highly curved regions, as observed in *ii* and *iv*. Nonetheless, even accounting for this discrepancy, the application of WDE still provides a significantly improved quantitative assessment compared to its absence.

4. Discussion and conclusion. The aim of this paper was to achieve automated calculation of morphological features using segmented images of macrophages, utilizing centers detected through cell tracking. Since there are some segmented fragments of macrophages, the completion of segmented fragments is essential for the

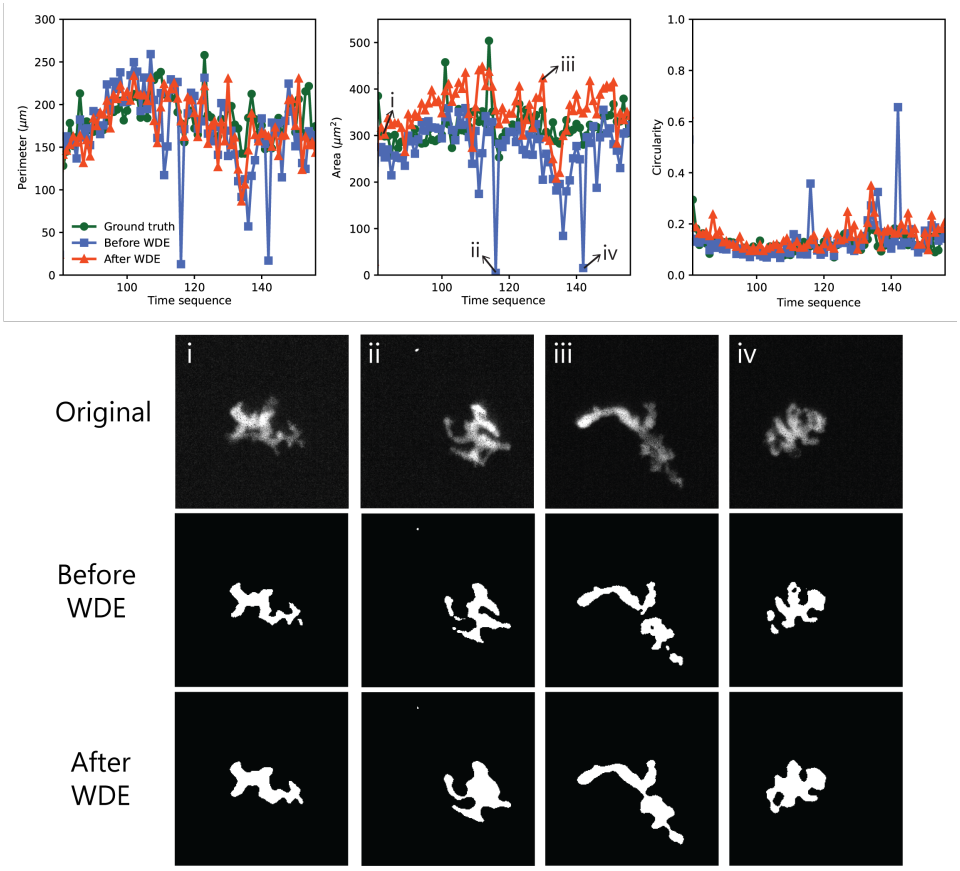

FIG. 3.5. *Morphological characteristics such as perimeter, area, and circularity are calculated over time for a macrophage exhibiting relatively complex shapes. Four time points, labeled as* i, ii, iii, iv*, are chosen to compare the segmented shapes before and after the application of weighted dilation and erosion.*

accurate computation of morphology. We presented a method involving weighted dilation and erosion using the level-set approach to complete these segmented fragments. The speed of level lines is regulated by the relationship between thresholds computed from the local Otsu's method and the original image intensity. We showed the effectiveness of the proposed approach in completing segmented fragments by preserving overall macrophage shapes across different shapes and intensity ranges. Ultimately, this method allowed for accurate quantitative evaluations. However, two limitations remain. First, in regions of high macrophage curvature, the method occasionally results in the smoothing out of such areas. Second, it is difficult to connect fragments that are too far apart. Despite the aforementioned limitations, the computed morphological features obtained from weighted dilation and erosion are precise enough as shown in several real examples. Furthermore, we expect that this approach could enhance tracking accuracy by employing a single center obtained from a completed segmented region, rather than relying on multiple centers for a single macrophage.

Acknowledgments. We thank Tamara Sipka, Mai Nguyen-Chi, and Georges Lutfalla at LPHI (Laboratory of Pathogen Host Interaction), CNRS, University of

Montpellier for providing the macrophage videos. This work has been supported by grants APVV-19-0460, APVV-23-0186, VEGA 1/0249/24, and the European Union's Horizon 2020 under EXCELLENT SCIENCE - Marie Skłodowska-Curie Actions with grant agreement ID 955576.

REFERENCES

[1] P. Friedl and B. Weigelin, *Interstitial leukocyte migration and immune function*, Nature Immunology, 9(9):960–969, 2008.

[2] E. Van Goethem, R. Poincloux, F. Gauffre, I. Maridonneau-Parini, and V. Le Cabec, *Matrix architecture dictates three-dimensional migration modes of human macrophages: differential involvement of proteases and podosome-like structures*, The Journal of Immunology, 184(2):1049–1061, 2010.

[3] F. O. Martinez and S. Gordon, *The M1 and M2 paradigm of macrophage activation: time for reassessment*, F1000prime reports, 6, 2014.

[4] M. Benoit, B. Desnues, and J.-L. Mege, *Macrophage polarization in bacterial infections*, The Journal of Immunology, 181(6):3733–3739, 2008.

[5] M. Hesketh, K. B. Sahin, Z. E. West, and R. Z. Murray, *Macrophage phenotypes regulate scar formation and chronic wound healing*, International Journal of Molecular Sciences, 18(7):1545, 2017.

[6] L. Alvarez, F. Guichard, P.-L. Lions, and J.-M. Morel, *Axioms and fundamental equations of image processing*, Archive for rational mechanics and analysis, 123:199–257, 1993.

[7] S. Osher and R. P. Fedkiw, *Level set methods: an overview and some recent results*, Journal of Computational Physics, 169(2):463–502, 2001.

[8] S. Osher and J. A. Sethian, *Fronts propagating with curvature-dependent speed: Algorithms based on Hamilton-Jacobi formulations*, Journal of computational physics, 79(1):12–49, 1988.

[9] Nobuyuki Otsu, *A threshold selection method from gray-level histograms*, Automatica, vol. 11, no. 285-296, pp. 23-27, 1975.

[10] S. A. Park, T. Sipka, Z. Krivá, G. Lutfalla, M. Nguyen-Chi, and K. Mikula, *Segmentation-based tracking of macrophages in 2D+ time microscopy movies inside a living animal*, Computers in Biology and Medicine, 153:106499, 2023.